Radiation Parameterization for Three-Dimensional Inhomogeneous Cirrus Clouds: Application to Climate Models

YU GU AND K. N. LIOU

Department of Atmospheric Sciences, University of California, Los Angeles, Los Angeles, California

(Manuscript received 8 March 2000, in final form 13 September 2000)

ABSTRACT

A three-dimensional (3D) radiative transfer model has been developed to simulate the transfer of solar and thermal infrared radiation in inhomogeneous cirrus clouds. The model utilizes a diffusion approximation approach (four-term expansion in the intensity) for application to inhomogeneous media, employing Cartesian coordinates. The extinction coefficient, single-scattering albedo, and asymmetry factor are functions of spatial position and wavelength and are parameterized in terms of the ice water content and mean effective ice crystal size. The correlated *k*-distribution method is employed for incorporation of gaseous absorption in multiple-scattering atmospheres. Delta-function adjustment is used to account for the strong forward-diffraction nature in the phase function of ice particles to enhance computational accuracy. Comparisons of the model results with those from plane-parallel (PP) and other 3D models show reasonable agreement for both broadband and monochromatic results. Three-dimensional flux and heating/cooling rate fields are presented for a number of cirrus cases in which the ice water content and ice crystal size are prescribed. The PP method is shown to be a good approximation under the homogeneous condition when the cloud horizontal dimension is much larger than the cloud thickness. As the horizontal dimension decreases, clouds produce less infrared warming at the bottom as well as less cooling at the top, while more solar heating is generated within the cloud. For inhomogeneous cases, upwelling and downwelling fluxes display patterns corresponding to the extinction coefficient field. Cloud inhomogeneity also plays an important role in determining both solar and IR heating rate distributions. The radiation parameterization is applied to potential cloud configurations generated from GCMs to investigate broken clouds and cloud-overlapping effects on the domain-averaged heating rates. Clouds with maximum overlap tend to produce less heating than those with random overlap. For the prescribed cloud configurations designed in this paper, broken clouds show more solar heating as well as more IR cooling as compared with a continuous cloud field.

1. Introduction

Cirrus clouds are globally distributed, being present at all latitudes and in all seasons with a global cloud cover of about 20%–30% and more than 70% in the Tropics (Wylie et al. 1994). The effects of cirrus clouds on the radiation budget of the earth and the atmosphere, and hence their impact on weather and climate processes, have been articulated by Liou (1986, 1992), Stephens and Tsay (1990), and Donner et al. (1997). Satellite mapping of the optical depth in midlatitude and tropical regions has illustrated that cirrus clouds are frequently finite in nature and display substantial horizontal variabilities (Minnis et al. 1993; Ou et al. 1995). Vertical inhomogeneity of the ice crystal size distribution and ice water content has also been demonstrated in the replicator sounding observations (Heymsfield and Miloshevich 1993) and the time series of backscattering coefficients derived from lidar returns (Sassen 1991; Spinhirne and Hart 1990). Since cirrus clouds are an important element in modulating the energy budget of the earth–atmosphere system, the potential effects of cloud geometry and inhomogeneity on the transfer of radiation must be carefully studied to understand their impact on the radiative properties of the atmosphere as well as to perform proper interpretations of radiometric measurements from the ground, the air, and space.

Most of the approaches to 3D radiative transfer employ the Monte Carlo method (e.g., Cahalan et al. 1994; O'Hirok and Gautier 1998). For application to cirrus clouds, Liou and Rao (1996) have used the successive orders of scattering (SOS) approach that can be directly applied to the specific geometry and inhomogeneous structure of a medium. Some other methods have also been presented, including the spherical harmonic method employed by Evans (1993) and the Fourier–Riccati approach by Gabriel et al. (1993) for radiative transfer in 2D inhomogeneous clouds. Evans (1998) has developed a spherical harmonics discrete-ordinates method (SHDOM) for modeling radiative transfer in inhomo-

Corresponding author address: Prof. K. N. Liou, Department of Atmospheric Sciences, University of California, Los Angeles, Los Angeles, CA 90095.
E-mail: knliou@atmos.ucla.edu

geneous three-dimensional media. Ou and Liou (1982) presented a spherical harmonic method in multiple dimensions, based on which the diffusion approximation for 3D radiative transfer can be developed (Liou 1992). However, the requirement of computer resources remains the primary obstacle in the modeling of 3D radiative transfer.

Radiative heating drives the dynamic and thermodynamic processes in the atmosphere. Radiative equilibrium at the top of the atmosphere represents the first approximation for climate. Since radiative heating is strongly regulated by clouds, knowledge and understanding of the optical and microphysical properties of cirrus clouds are essential for the development of radiation parameterizations for incorporation in climate models. In conjunction with our objective of understanding the effects of 3D inhomogeneous cirrus on radiative flux and heating rate profiles in the atmosphere and of providing a physical basis for parameterization in climate models, we have developed a 3D inhomogeneous radiative transfer model based on a modified diffusion approximation employing Cartesian coordinates. In section 2, we describe the model in detail and compare the monochromatic results with those computed from plane-parallel (PP) and other methods. Section 3 illustrates the effects of cloud geometry and inhomogeneity on the distribution of radiative fluxes and heating rates. Application of the radiation parameterization to climate model studies is discussed in section 4. Summaries are given in section 5.

2. A 3D inhomogeneous radiative transfer model

a. Diffusion approximation

The general equation governing the transfer of diffuse intensity I can be expressed in the form

$$-\frac{dI(\mathbf{s}, \mathbf{\Omega})}{\beta_e(\mathbf{s})ds} = I(\mathbf{s}, \mathbf{\Omega}) - J(\mathbf{s}, \mathbf{\Omega}), \tag{1}$$

where $\mathbf{s}$ is the position vector; $\mathbf{\Omega}$ is a unit vector representing the angular direction of scattering through the position vector; and β_e is the extinction coefficient for cloud particles, which is a function of the position vector. The source function, which is produced by the single scattering of the direct solar irradiance, multiple scattering of the diffuse intensity, and emission of the cloud, can be written as follows:

$$J(\mathbf{s}, \mathbf{\Omega}) = \frac{\varpi(\mathbf{s})}{4\pi} P(\mathbf{s}; \mathbf{\Omega}, \mathbf{\Omega}_0) F_\odot e^{-\tau_s} + \frac{\varpi(\mathbf{s})}{4\pi} \int_{4\pi} I(\mathbf{s}, \mathbf{\Omega}') P(\mathbf{s}; \mathbf{\Omega}, \mathbf{\Omega}')\, d\mathbf{\Omega}' + [1 - \varpi(\mathbf{s})] B(T), \tag{2}$$

where $\varpi = \beta_s/\beta_e$ is the single-scattering albedo with β_s the scattering coefficient; the phase function P is defined by the position vector and the incoming and outgoing solid angles $\mathbf{\Omega}'(\mathbf{\Omega}_0)$ and $\mathbf{\Omega}$, respectively; $F_\odot$ is the incident solar irradiance; τ_s is the optical depth in the direction of the incident solar beam; and $B(T)$ is the Planck function of temperature T. Applicability of the source function to solar and thermal infrared regions is dependent on wavelength.

By expanding the phase function and the intensity in terms of spherical harmonic functions and by taking four terms in the expansion in a manner presented in Liou and Ou (1979) and Liou (1992), the following 3D inhomogeneous diffusion equation can be derived in the form

$$\nabla \cdot (\nabla I_0^0/\beta_t) - 3\alpha_t I_0^0 = -F_t + \mathbf{\Omega}_0 \cdot \nabla(F_t g/\beta_t), \tag{3}$$

where

$$\beta_t = \beta_e(1 - \varpi g), \tag{4}$$

$$\alpha_t = \beta_e(1 - \varpi), \tag{5}$$

$$F_t = \begin{cases} 3\beta_e F_\odot e^{-\tau_s}/4\pi, & \text{solar} \\ 3\beta_e(1 - \varpi)B(T), & \text{IR.} \end{cases} \tag{6}$$

In these equations, all the variables are functions of the coordinate (x, y, z); I_0^0 is the first component of the intensity expansion; β_t and α_t are terms associated with the single-scattering properties; g is the asymmetry factor; F_t is associated with the direct solar radiation and emission of the cloud, respectively, depending on the wavelength; and the last term in Eq. (3) vanishes for IR bands. Since the basic radiative transfer equation cannot be solved analytically, numerical methods must be used.

b. Numerical method

With the diffusion approximation, the basic radiative transfer equation now transforms into a general second-order partial differential equation, in which all the coefficients are dependent on the position vector. These types of equations are usually solved by linearization and iteration when they are nonlinear. We have approached the solution of the system of equations by using a finite-difference method. In this approach, the spatial variations in the I_0^0 field and the optical properties are represented by discretization on a grid. The central differential scheme with a second-order accuracy is employed for all partial differential terms in Eq. (3). The solution of the equation also requires the imposition of boundary conditions, which are set in such a manner that the incident diffuse flux at each surface is equal to zero or a constant. After applying the finite-difference scheme, the problem of solving the diffusion equation reduces to the solution of a large sparse linear system. The finite-difference form of the model equation is given by

$$a_{11}I_0^0(i+1,j,k) + a_{12}I_0^0(i-1,j,k) + a_{21}I_0^0(i,j+1,k) + a_{22}I_0^0(i,j-1,k) + a_{31}I_0^0(i,j,k+1) + a_{32}I_0^0(i,j,k-1) + eI_0^0(i,j,k) = f(i,j,k), \quad (7)$$

where

$$a_{i1,2} = 1/\beta_t(x_i \pm \Delta x_i/2, \sim), \quad (8)$$

$$e = -\left\{\sum_{i=1}^{3} [1/\beta_t(x_i + \Delta x_i/2, \sim) + 1/\beta_t(x_i - \Delta x_i/2, \sim)] + 3\alpha_t\right\}, \quad (9)$$

with x_i ($i = 1, 2, 3$) representing x, y, and z, respectively; the symbol "$\sim$" used to represent the other two dimensions; and $f(i, j, k)$ denoting the right-hand-side terms in Eq. (3).

There are roughly three different approaches that can be employed to solve Eq. (7), including the relaxation, Fourier, and direct matrix methods. The direct matrix method generally requires a large amount of computer storage and is not a good choice for grids larger than 10^4, while the Fourier method can only be used for equations with constant coefficients. Thus, we use the successive overrelaxation (SOR) method to calculate I_0^0 at each grid point. We can define the residual at any stage of the iteration as follows:

$$\mathrm{res}(i,j,k) = a_{11}I_0^0(i+1,j,k) + a_{12}I_0^0(i-1,j,k) + a_{21}I_0^0(i,j+1,k) + a_{22}I_0^0(i,j-1,k) + a_{31}I_0^0(i,j,k+1) + a_{32}I_0^0(i,j,k-1) + eI_0^0(i,j,k) - f(i,j,k). \quad (10)$$

The SOR algorithm for the solution of I_0^0 is then given by

$$I_0^0(i,j,k)^{(n)} = I_0^0(i,j,k)^{(n-1)} - \gamma\frac{\mathrm{res}(i,j,k)}{e}, \quad (11)$$

where n is the order of iterations and γ ($1 < \gamma < 2$) is an overrelaxation parameter used to achieve an efficient convergence (Rigal 1979). The norm of the residual res(i, j, k) can be used as a criterion for terminating the iteration.

Once I_0^0 is determined, the diffuse intensity and flux can then be obtained by

$$I(x,y,z;\mathbf{\Omega}) = I_0^0(x,y,z) - \frac{3}{2h\beta_e}\sum_{i=1}^{3}\frac{\partial I_0^0(x,y,z)}{\partial x_i}\Omega_{x_i} + \frac{9q}{2h}(\mathbf{\Omega}\cdot\mathbf{\Omega}_0)e^{-\tau_s}, \quad (12)$$

$$F_{\pm x_i}(x,y,z) = \int_{2\pi} I(x,y,z;\mathbf{\Omega})\Omega_{x_i}\,d\Omega, \quad (13)$$

where $h = 3(1 - \varpi g)/2$; $q = \varpi g F_\odot/12\pi$; $x_1 = x$, $x_2 = y$, $x_3 = z$; $\Omega_x = (1 - \mu_0^2)^{1/2}\cos\phi$; $\Omega_y = (1 - \mu_0^2)^{1/2}\sin\phi$; and $\Omega_z = \mu_0$. For thermal infrared radiation, the last term in Eq. (12) vanishes. The local rate of change of temperature is produced by the 3D radiative flux divergence in the form

$$\frac{\partial T}{\partial t}(x,y,z) = -\frac{1}{c_p\rho_a}\nabla\cdot\mathbf{F}, \quad (14)$$

where $\mathbf{F} = \mathbf{i}F_x + \mathbf{j}F_y + \mathbf{k}F_z$, ($\mathbf{i}$, $\mathbf{j}$, $\mathbf{k}$) are the unit vectors, and F_x, F_y, and F_z are the net fluxes in the x, y, and z directions, respectively.

c. Delta adjustment and parameterization of the single-scattering properties

To increase computational accuracy, we have applied the similarity principle for radiative transfer to each grid point such that

$$\beta_e^* = \beta_e(1 - \varpi f), \quad (15)$$

$$\varpi^* = \varpi(1 - f)/(1 - \varpi f), \quad (16)$$

$$g^* = (g - f)/(1 - f). \quad (17)$$

The fractional energy in the diffraction peak of the phase function f is taken to the $\varpi_4/9$, where ϖ_4 is the fourth moment in the phase function expansion. It can be proven that the radiation transfer equation after the scaling adjustment is exactly the same as Eq. (2), except that β_e, ϖ, and g are replaced by β_e^*, ϖ^*, and g^*. Calculations of the single-scattering properties require a light scattering program and information about ice crystal size distributions. The required calculations are usually tedious and time consuming. For this reason, we follow the parameterization approach developed by Fu and Liou (1993) in determining the single-scattering properties. The extinction coefficient, single-scattering albedo, and asymmetry factor, which are functions of the position vector and wavelength, can be parameterized in terms of the ice water content (IWC) and mean effective ice crystal size D_e as follows:

$$\beta_e(\lambda;x,y,z) = \mathrm{IWC}(x,y,z)\sum_{n=0}^{N} a_n(\lambda) \div D_e^n(x,y,z), \quad (18)$$

$$1 - \varpi(\lambda;x,y,z) = \sum_{n=0}^{N} b_n(\lambda)D_e^n(x,y,z), \quad (19)$$

$$g(\lambda;x,y,z) = \sum_{n=0}^{N} c_n(\lambda)D_e^n(x,y,z), \quad (20)$$

where a_n, b_n, and c_n are certain coefficients that must be determined from numerical fitting based on "exact" light scattering and absorption calculations for a range of ice crystal size distributions and shapes. Fu and Liou (1993) have found that $N = 1$–2 is sufficient in these parameterizations to achieve an accuracy within 1% in

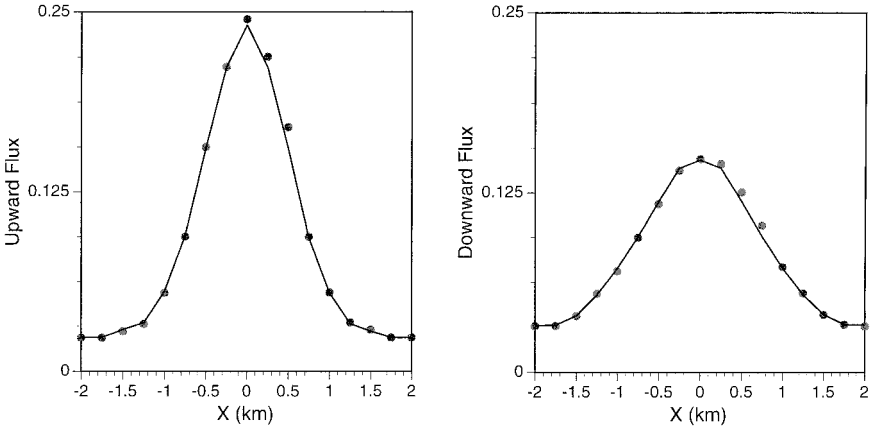

FIG. 1. Comparison of the upwelling and downwelling fluxes of a 2D conservative and isotropic medium computed from the present model with the results from the SOS approach presented by Liou and Rao (1996).

the fitting. Once the 3D spectral single-scattering properties are defined, the 3D inhomogeneous diffusion equation can then be solved numerically, as described in the previous section. Flux and heating rate profiles can subsequently be evaluated as functions of the spatial coordinates (x, y, z). Although our prime application is for cirrus clouds, the conceptual approach of parameterization should be applicable to general cloud fields.

3. Testing the model and application to cirrus cloud fields

In the following, we first check the accuracy of the 3D radiative transfer model. Liou and Rao (1996) have employed an SOS method for the calculations of 3D radiative transfer. The results obtained from this method agree well with those determined from other 3D and Monte Carlo programs. The Monte Carlo approach is normally considered to be the exact method in multidimensional radiative transfer problems, although its accuracy is dependent on the number of photons employed in the calculations. We compare the results computed from the modified diffusion approximation approach with those presented by Liou and Rao (1996). We select a 2D case in which the extinction coefficient field is described by a Gaussian function: $\beta_e(x, z) = 2z/z_c \exp[-\pi(x - x_c/2)^2]$, where z_c and x_c are the cloud thickness and the dimension in the x direction, respectively. The solar zenith angle is set to be 30°, and the scattering is assumed to be conservative and isotropic. Figure 1 shows comparison of the normalized upwelling and downwelling diffuse fluxes for the SOS and the modified diffusion approximation methods. The computed fluxes are almost but not exactly symmetric with respect to the central point due to the 30° solar zenith angle used in the calculation. The maximum and minimum patterns are associated with the periodic behavior of the extinction coefficient field. The present results are in excellent agreement with those from the SOS method with differences that cannot be distinguished from the curves.

Next, we compare the flux and heating rate profiles for a typical homogeneous cirrus cloud case using the 0.63- and 2.22-μm wavelengths. A mean extinction coefficient with a value of 0.381 km^{-1}, which is obtained from the First International Satellite Cloud Climatology Project (ISCCP) Regional Experiment-Intensive Field Observation (IFO) data for cirrostratus, is used along with a solar zenith angle of 30°. The single-scattering albedo is close to 1 for the 0.63-μm wavelength, while it is 0.9185 for the 2.22-μm wavelength. Figure 2 shows the normalized upward, downward, and net fluxes within the cloud for the two wavelengths, together with the heating rate profile for 2.22 μm computed from the 3D radiative transfer model and 1D PP method. The normalized downward flux is 1 at the top, while the normalized upward flux is 0 at the cloud base. Since the cloud has little absorption at the 0.63-μm wavelength, the vertical net flux is nearly constant. At the 2.22-μm wavelength, the net fluxes decrease with cloud depth resulting in heating within the cloud because ice crystals absorb a substantial solar flux at this wavelength. When the horizontal dimension becomes larger, results for the 3D case approach those for the 1D case.

Verification of the total solar and IR heating rates computed from any 3D inhomogeneous radiative transfer program would be difficult because prior results do not exist. Thus, we compare the domain-averaged solar and IR heating rates computed from a 3D homogeneous cirrus with those computed from Fu and Liou's program for the PP counterpart. For the spectral integration, we have followed the approach developed by Fu and Liou (1993). The entire spectrum is divided into 6 solar bands and 12 IR bands covering the absorption due to various gases. Using the correlated k-distribution method (Fu and Liou 1992; Liou et al. 1998), a total of 121 spectral calculations are required for each 3D profile. To con-

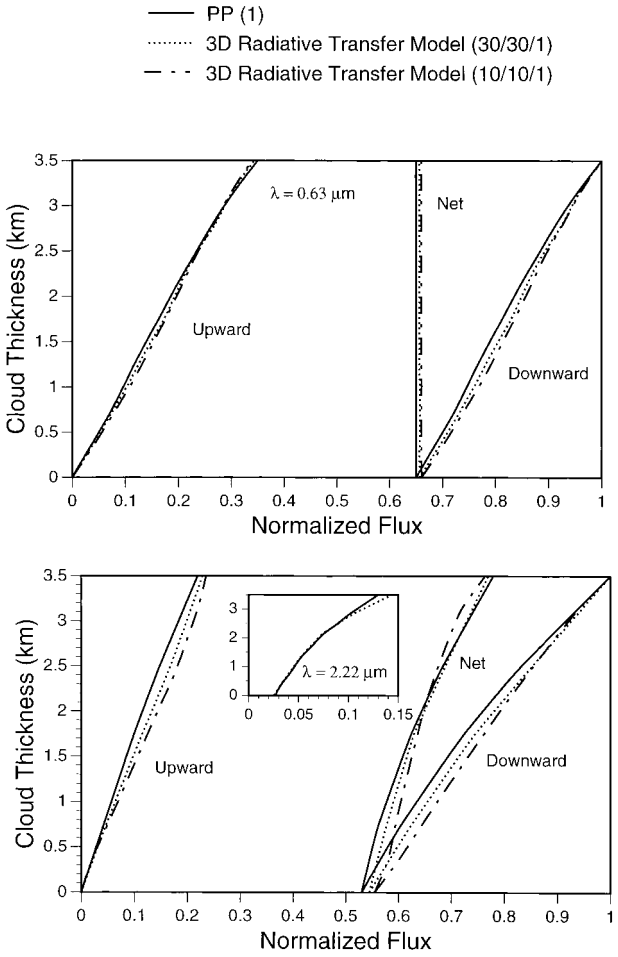

FIG. 2. Comparison of the normalized upward, downward, and net fluxes for the 0.63- and 2.22-μm wavelengths and heating rates for 2.22-μm wavelength computed from the present 3D model and PP method.

struct a homogeneous cirrus cloud, a uniform value of 0.015 g m^{-3} for ice water content is used for each grid point, while the mean effective ice crystal size is taken as 25 μm.

Similar to the monochromatic calculation, we would expect that under the homogeneous condition, the broadband results derived from the 3D model should approach those from the PP method if the horizontal dimension is much larger than the vertical. Indeed, as shown in Fig. 3, for a relative dimension of 5/5/1, the domain-averaged cloud heating rates computed from the 3D model are close to those computed from the PP program. Comparison results are similar for other mean effective ice crystal sizes, with larger D_e having smaller emittance/absorptance and hence smaller radiative heating gradients. This comparison not only shows the physical reliability of the present 3D model but also implies that the PP method is a rather good approximation for a homogeneous cloud condition where the cloud horizontal scale is much larger than the vertical. In the following, we apply the model to investigate the effects of finite, inhomogeneous cirrus clouds on the distribution of heating within the cloud.

It has been shown from Figs. 2 and 3 that for both monochromatic and broadband calculations, distributions of the flux and heating rate for the 3D case approach those for the PP case when the horizontal dimension in the former case is much larger than the vertical dimension. The effect of cloud finiteness on heating rates can be clearly seen in Fig. 3. As the horizontal dimension decreases, clouds tend to produce less IR cooling at the top as well as less IR warming at the bottom, and generate more solar heating within the cloud, due primarily to the effect of finite dimension. Fu et al. (2000) formulated a 3D broadband radiative transfer scheme by integrating a 3D Monte Carlo photon transport algorithm into the Fu–Liou radiation model,

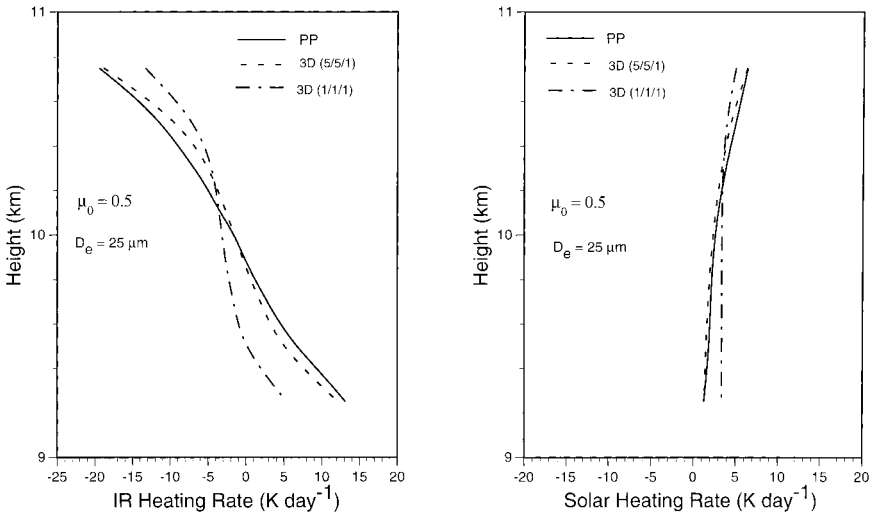

FIG. 3. Comparison of the broadband IR and solar heating rates calculated from the 3D model and the PP method in a homogeneous cirrus cloud.

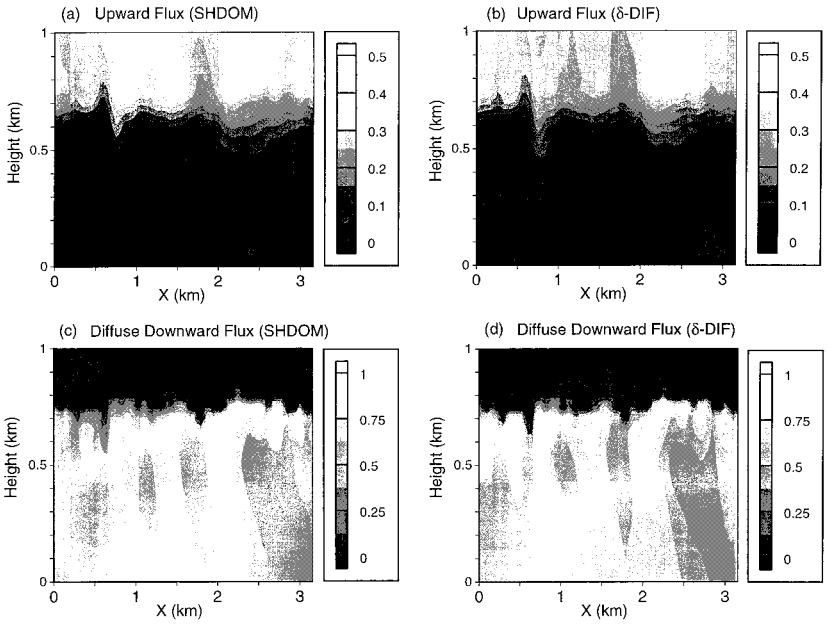

FIG. 4. Comparisons of the upward and diffuse downward fluxes calculated from (a) and (c) SHDOM and (b) and (d) the present 3D radiation model employing a 2D slice of an LES model–simulated cloud field.

and found that cloud geometry effects enhance slightly the atmospheric solar absorption regardless of solar zenith angle for the tropical convective cloud system. Using a Monte Carlo–based 3D model, O'Hirok and Gautier (1998) also found that the 3D effect produces more solar absorption and that the PP method for clouds used in GCMs can underestimate atmospheric absorption as a result of this effect. However, some other studies have showed less absorption for 3D calculations (e.g., Davies et al. 1984; Hignett and Taylor 1996). The differences between model results are believed to be due primarily to differences in cloud morphologies and boundary conditions used in the models, as well as the definition of the absorption considered (cloud or cloudy column).

We have made further comparisons with the results computed from the SHDOM method (Evans 1998) using a 2D slice of a realistic cloud field obtained from a large eddy simulation (LES) of a stratocumulus (Moeng et al. 1996). A detailed description of this cloud and its radiative properties has been given in Evans (1998) and will not be duplicated here. The radiation calculations were carried out for the 1.65-μm wavelength using a solar zenith angle of 45° and a surface albedo of 0.06. The incident flux at the top of the domain is assumed to be unity. Figure 4 shows the upward and diffuse downward fluxes computed from SHDOM and the present 3D delta diffusion (δ-DIF) model. The present δ-DIF model produces flux fields that closely resemble those computed from SHDOM for this highly inhomogeneous cloud field. It is not surprising that those two methods compare rather well since both use the spherical harmonics expansion technique. The root-mean-square differences over the field normalized by the mean of the field are 0.0969 and 0.0584 for the upward and total downward fluxes, respectively. The downward flux difference is smaller because of the inclusion of the direct solar flux component. Last, it should be pointed out that the ''absolute'' accurate 3D inhomogeneous radiative transfer method has not been developed and accepted at this point, and it is a subject of a contemporary intercomparison research project.

In the following, we examine the cloud inhomogeneity effect on the distribution of heating rate. To define horizontal inhomogeneity, we use the optical depth and mean effective ice crystal size over an area of 30 km by 20 km near Coffeyville, Kansas, on 5 December 1991, retrieved from the advanced very high resolution radiometer (AVHRR) data. The optical depth in this area varies from 0.5 to 3, revealing that this cirrus cloud system was horizontally inhomogeneous. The horizontal extinction coefficient field can then be constructed from the optical depth and mean effective ice crystal size. Moreover, the extinction coefficient also varies in the vertical and can be estimated from the ice crystal data determined from the replicator sounding. By combining the satellite and replicator sounding data, a 3D IWC and mean effective ice crystal size field can be constructed (Liou and Rao 1996). It follows from Eqs. (18)–(20) that the extinction coefficient, single-scattering albedo, and asymmetry factor as functions of wavelength can be parameterized for inputs to the 3D inhomogeneous radiative transfer program. Figures 5a,b show the constructed IWC field in the horizontal plane (averaged over the height) and the latitude–height plane (averaged over

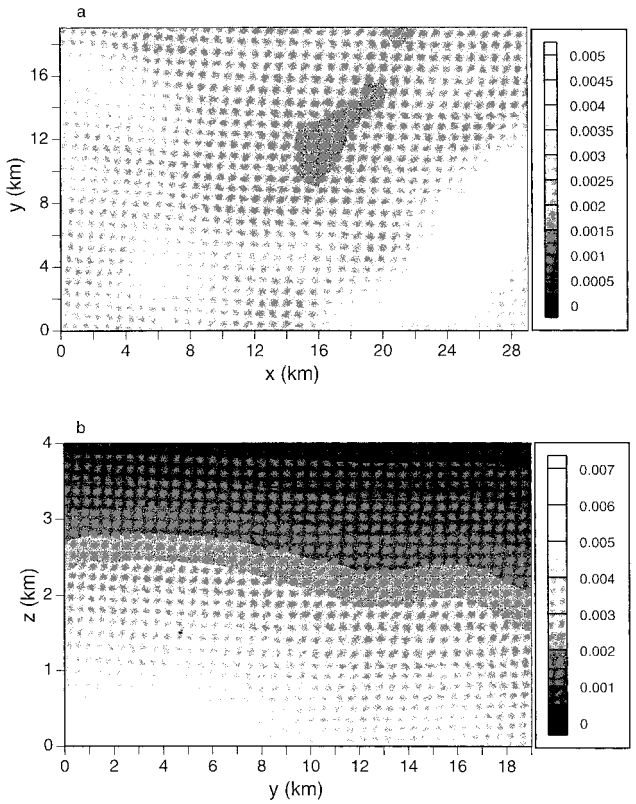

FIG. 5. The IWC (g m^{-3}) field constructed from AVHRR data over the area near Coffeyville, Kansas, on 5 Dec 1991 (Ou et al. 1995). (a) IWC is presented in the horizontal plane (averaged over the height); (b) IWC is shown in the latitude and height plane (averaged over the longitude).

the longitude), respectively. The value of the IWC field varies from 0.5 to 5 mg m^{-3} in the horizontal and from 1 to 7 mg m^{-3} in the vertical, indicating that this cirrus cloud system was horizontally and vertically inhomogeneous. For the homogeneous condition, mean single-scattering parameter values were used in the calculations. The solar zenith angle in this case is about 60°.

Figure 6 displays the differences in the averaged heating rates in the *x–y* and *y–z* planes between inhomogeneous and homogeneous clouds. In the *x–y* plane, the patterns correspond to the variabilities of the horizontal extinction coefficient (or IWC) field. More solar heating and IR warming are found in the area with larger extinction coefficients, while less solar heating and more IR cooling are shown in the area with smaller extinction coefficients. In the *y–z* plane, stronger IR cooling at the cloud top and slightly more IR warming at the bottom are displayed in the inhomogeneous case. This is associated with smaller extinction coefficients in the upper part of the cloud and larger values in the lower part of the inhomogeneous cirrus cloud. For solar radiation, more heating is found in the inhomogeneous case in the whole *y–z* plane.

Furthermore, we have carried out heating rate calculations for this cirrus cloud field using PP method (or the independent column approximation, which applies the plane-parallel radiation model to each column of the cloud field). Figures 7 and 8 show the averaged heating rates in the *x–y* and *y–z* planes computed from the 3D and PP models for solar and IR, respectively. Results from the 3D model are in general agreement with those from PP model, where the heating rate patterns are associated with the horizontal and vertical extinction coefficient fields. The differences for solar and IR heating rates between 3D and PP models are further illustrated in Fig. 9. In the *x–y* plane, more (less) solar heating and IR warming are shown in the 3D model in the area with larger (smaller) extinction coefficients. These difference patterns are in line with those reported by Liou and Rao (1996) for reflection function, transmission function, reflectance, and transmittance for 0.63- and 2.22-μm wavelengths. In the *y–z* plane, the difference pattern for IR is also associated with the variabilities of the vertical extinction coefficient (or IWC) field. For solar radiation, more solar heating is seen in the 3D model in the upper-left region, while less in the lower-right part, associated with the solar zenith angle. The differences between 3D and PP models for this particular cloud (30 km $\times$ 20 km $\times$ 3.5 km domain) have similar patterns in comparison with those between inhomogeneous and homogeneous cases, except that the quantities are much smaller. This implies that the PP method tends to smooth the radiation field for highly horizontally inhomogeneous media.

We also examine the efficiency of the present 3D model as compared with the PP model. Since the latter (e.g., the Fu–Liou program) must perform radiation calculations column by column, a total of 30 $\times$ 20 column calculations is required for this 3D cloud case. Although the Fu–Liou program takes only about 1–2 s for one broadband calculation, calculations for the total cloud field requires about 12–15 min on a Sun workstation. The present 3D model, on the other hand, takes only about 4 min for this case.

4. Application to climate models

The formation of partial cloudiness and its consequence of vertical overlap appear to become a contemporary issue in the development of climate models. The most straightforward approach to dealing with the partially cloudy case is to assume either random or maximum overlap. The sky is then divided into sections, within which clouds are taken as a homogeneous layer with cloud amount equal to either 0 or 1. Radiative fluxes are calculated for each section and then weighted by the cloud amount to derive the total fluxes (Chou et al. 1998). Random overlap assumes that all cloud layers are independent and therefore tends to produce a larger total cloud cover since it neglects cloud geometric association. The configuration requires 2^n sets of calculations, where n is the number of total cloud layers, and thus would involve a large amount of computational

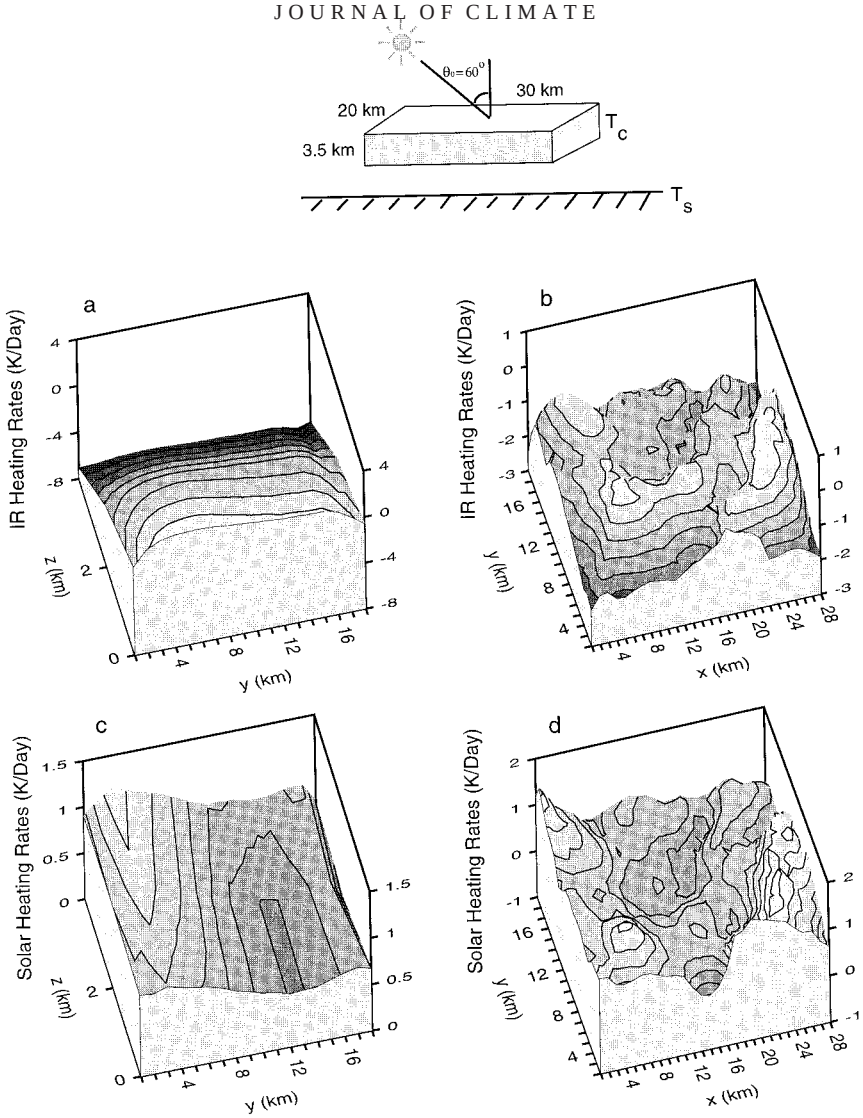

FIG. 6. The 3D images of the differences in (a) and (b) IR and (c) and (d) solar heating rates (K day^{-1}) between inhomogeneous and homogeneous cirrus cloud layers. Results in (a) and (c) are presented in the latitude and height plane (averaged over the longitude or x direction), while (b) and (d) are shown in the horizontal plane (averaged over the height).

effort. Geleyn and Hollingsworth (1979) proposed a mixed overlap treatment by assuming that adjacent cloud layers share maximum overlap while discrete clouds are randomly overlapped. This approach has been shown to better match observations (Tian and Curry 1989). Stubenrauch et al. (1997) implemented a horizontal subgrid cloud overlap scheme in a GCM, in which cloud blocks were formed by adjacent cloud layers using maximum overlap, while different cloud blocks separated by a level of clear sky were assumed to randomly overlap. This subgrid cloud structure allows determination of the occurrence probabilities of columns with different vertical structures in each horizontal grid cell. The PP radiative flux calculations can then be carried out for each column. The PP method (or independent column approximation) is a good approximation for clear or overcast cloud fields. However, for clouds with inhomogeneous composition and structure, horizontal radiative flux differentials could be an important factor in determining heating rate distribution.

The present 3D radiative transfer model allows us to examine cloud overlapping effects on domain-averaged heating rates, an important parameter in climate models, defined by

$$\overline{\left(\frac{\partial T}{\partial t}\right)} = \frac{1}{MN}\sum_{i=1}^{M}\sum_{j=1}^{N}\left(\frac{\partial T}{\partial t}\right)_{i,j}, \tag{21}$$

where M and N are the total grid points in the x and y directions, respectively. We may also investigate the effects of broken cloud fields on the radiative heating rate distribution. At the surface, we set a two-dimensional

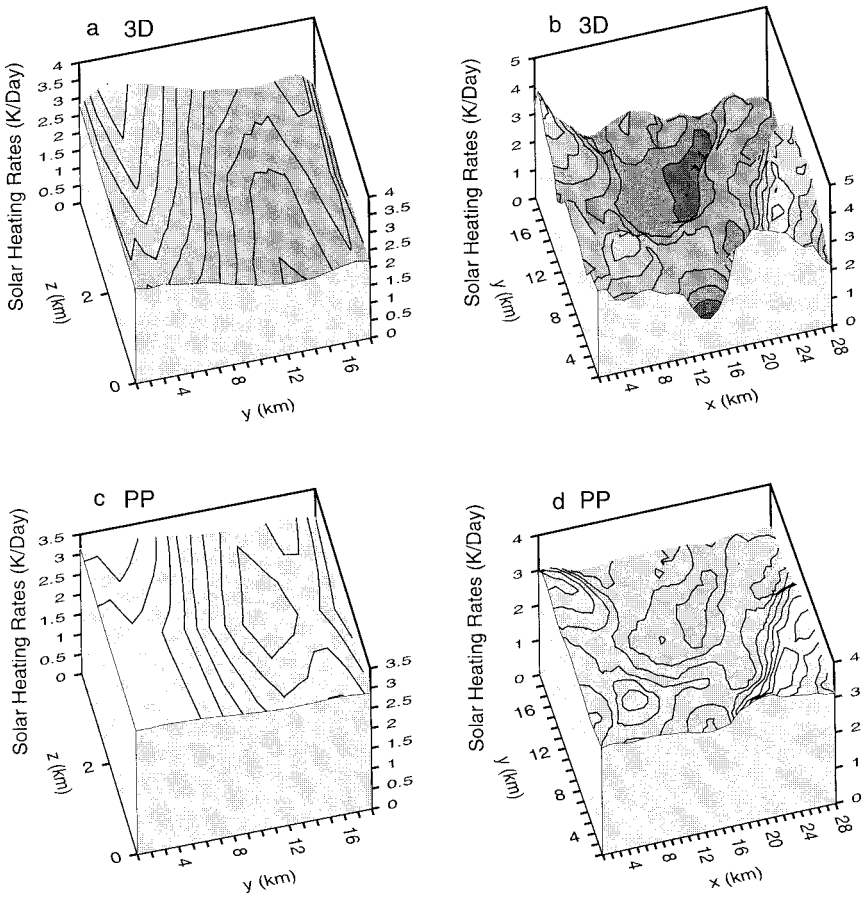

FIG. 7. The 3D images of the solar heating rates (K day^{-1}) calculated from the (a) and (b) 3D model and (c) and (d) plane-parallel model. Results in (a) and (c) are presented in the latitude and height plane (averaged over the longitude or x direction), while (b) and (d) are shown in the horizontal plane (averaged over the height).

surface albedo so that an upward solar flux reflected from the surface at the lower boundary can be taken into account. For the upper boundary, the direct solar flux at the top of atmosphere is attenuated to the position of the top model domain.

Three experiments are designed for cloud overlap study, as shown in Figs. 10a–c, which display a number of possible distributions for low, middle, and high clouds, leading to different numbers of columns. Two experiments designed to investigate broken cloud effects are shown in Figs. 10d and 10e. The PP model requires N calculations, where N is indicated in the diagrams. However, the 3D model only requires one calculation for each grid box to obtain heating rates involving an overlap configuration.

Application of the 3D inhomogeneous radiative transfer model to partly cloudy conditions or broken cloud fields may encounter computational problems since the mean photon free path length is much longer than the scale of spatial variations in the optical properties at the cloud/clear interface. A proper adjustment is therefore required in clear sky where the δ adjustment for the Rayleigh phase function is not applicable. We solve this problem by adding a background aerosol distribution, which represents a more realistic clear condition and, at the same time, the Lorenz–Mie scattering will allow an adjustment of the photon free path length. This method has proven to be successful in achieving numerical stability, particularly for application to broken clouds. Figure 11 shows a comparison of the solar and IR heating/cooling rates computed from the PP approach and the 3D model for one layer of broken clouds with a fractional cover of 60%. The two sets of results are similar in the heating rate profile, except for the differences produced by the effects of cloud geometry noted previously.

To investigate cloud overlap effects, we classify the input cloud fields in three types: high, middle, and low clouds. Each cloud is considered to be homogeneous with a thickness of 1 km and a cloud fractional cover of 60%. The mid- and low-level clouds are composed of liquid water, while the high-level cloud consists of ice particles. The liquid/ice water contents (LWC/IWC) and mean effective particle sizes (r_e/D_e) are prescribed.

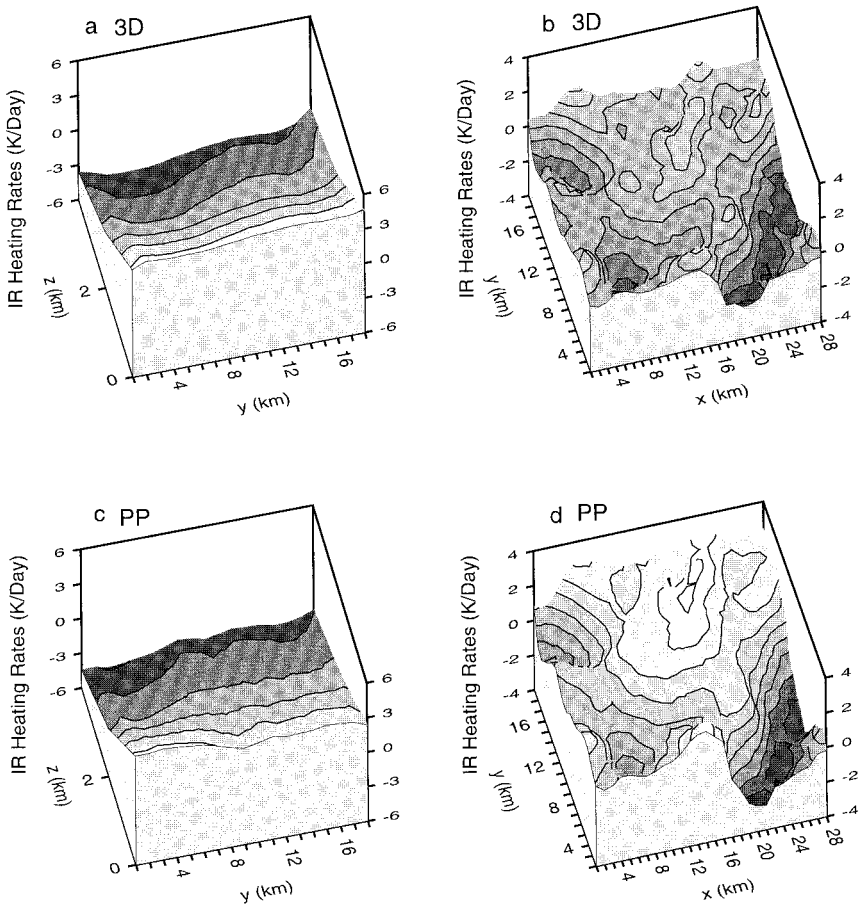

FIG. 8. The 3D images of the IR heating rates (K day^{-1}) calculated from the (a) and (b) 3D model and (c) and (d) plane-parallel model. Results in (a) and (c) are presented in the latitude and height plane (averaged over the longitude or x direction), while (b) and (d) are shown in the horizontal plane (averaged over the height).

A value of 0.2 g m^{-3} is set for LWC and 4.0 μm for r_e, while 0.015 g m^{-3} and 25 μm are used for IWC and D_e, respectively. The corresponding optical depths for the liquid and ice cloud layers are about 60 and 2, respectively. The surface albedo $\alpha(x, y)$ is assumed to be uniform with a value of 0.1. Figures 10a and 10c correspond to maximum (with a total cloud cover $\eta = 60\%$) and random ($\eta = 97.6\%$) overlap, respectively, while Fig. 10b represents the cloud structure with maximum overlap for mid- and low-level clouds and random overlap between high cloud and the two-combined cloud field ($\eta = 88\%$). The solar zenith angle is taken to be 60° in these calculations to highlight the 3D effect.

Domain-averaged solar heating rates for each cloud overlap calculated from the PP method are shown in Fig. 12a. The heating rate patterns for the three cloud configurations are in general agreement, except at the top of the mid- and low-level clouds where maximum overlap produces less heating because of a smaller cloud cover. The heating profiles computed from the 3D model, however, show substantial differences. Heating rates produced from maximum overlap are significantly smaller than those from the other two overlap configurations in the middle cloud, with the largest value being produced by complete random overlap, and are slightly greater in the high cloud. Clouds with random overlap produce larger total cloud cover and consequently generate more heating than those with maximum overlap, especially for a large solar zenith angle. These results are in general agreement with the conclusions obtained by Morcrette and Fouquart (1986), Liang and Wang (1997), and Barker et al. (1999).

Comparisons of the heating rate results between 3D and PP models are displayed in Figs. 12c–e. Heating rates obtained from the 3D model are greater than those from the PP method for high cloud in maximum overlap, and less in the other two configurations, and are all less for low cloud and the atmosphere. The differences are more pronounced for larger solar zenith angles because photons can enter through cloud sides and be trapped within the cloud. It is interesting to note that while heating within the middle cloud is significantly greater

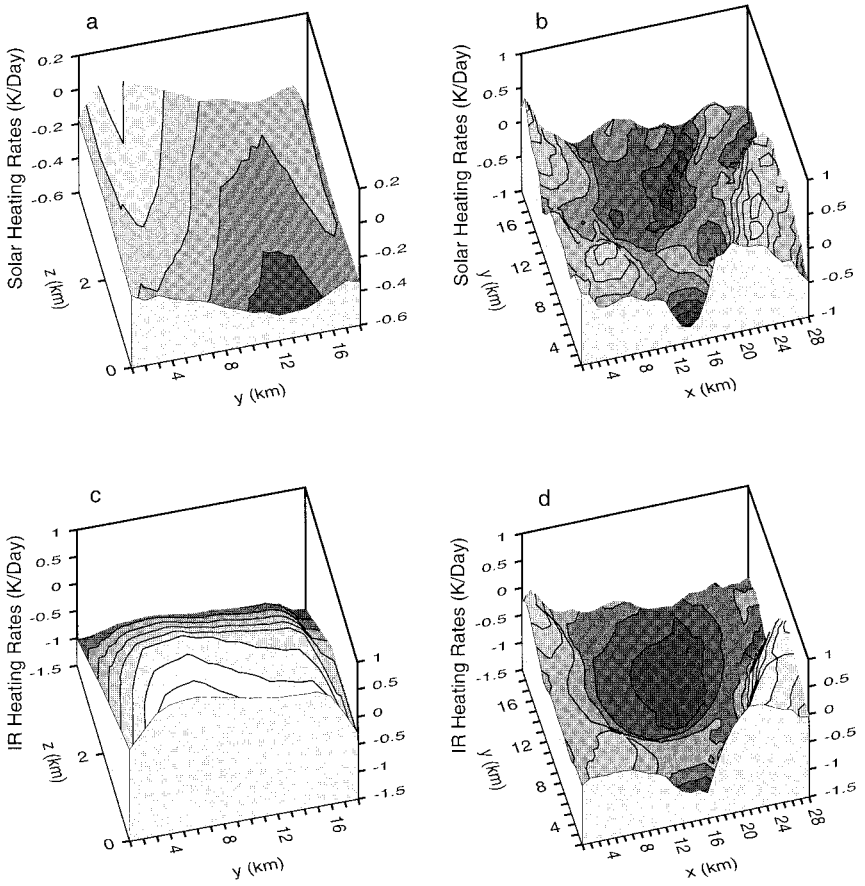

FIG. 9. The 3D images of the differences in (a) and (b) solar and (c) and (d) IR heating rates (K day^{-1}) between the 3D and plane-parallel models. Results in (a) and (c) are presented in the latitude and height plane (averaged over the longitude or x direction), while (b) and (d) are shown in the horizontal plane (averaged over the height).

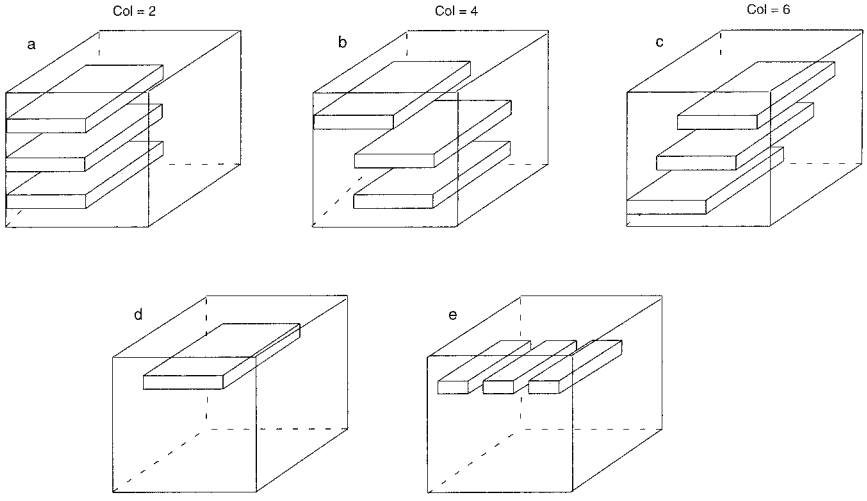

FIG. 10. Potential cloud configurations generated from GCMs. Distributions of the distinct possible positions for high, middle, and low clouds are displayed in (a)–(e): (a) two columns, (b) four columns, (c) six columns, (d) continuous cloud field, and (e) broken clouds.

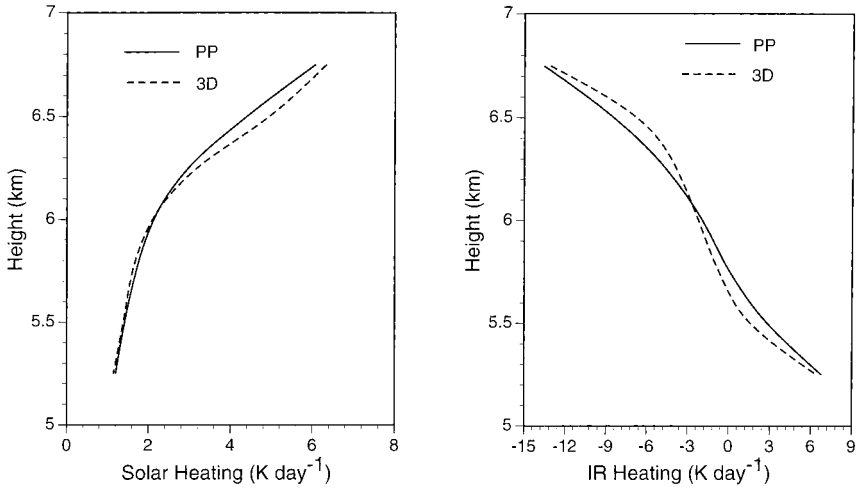

FIG. 11. (a) Solar and (b) IR heating rates computed from PP method (solid) and 3D radiative transfer model (dashed) for one level of broken clouds with a cloud amount of 60%.

for four- and six-column cloud configurations, heating results for two column, that is, maximum overlap, are smaller than those from the PP case. Thus, how the clouds are vertically positioned is critically important in the determination of heating/cooling rates. Some other researchers have also arrived at similar conclusions. Morcrette and Fouquart (1986) found that different cloud overlaps employed in a solar radiation scheme result in differences in initial radiative forcing, and may lead to different simulated climate states. Liang and Wang (1997) also showed that the vertical distribution of clouds significantly affects radiative heating/cooling distributions. Thus, climate simulations from GCMs could be sensitive to the treatment of cloud overlap. It is an issue that requires considerable research and development for solution.

In comparison with solar heating rates, domain-averaged IR heating/cooling rates show relatively smaller differences among different cloud configurations in both 3D and PP models. However, larger IR cooling is produced in the low cloud for random overlap configuration, while slightly smaller IR cooling is generated in the middle cloud for maximum overlap configuration in the PP case, primarily associated with cloud covers. Results from the 3D and PP models show significant differences. The 3D clouds produce less IR cooling at the cloud top and less IR warming at the cloud bottom, as compared with PP clouds as a result of cloud ge-

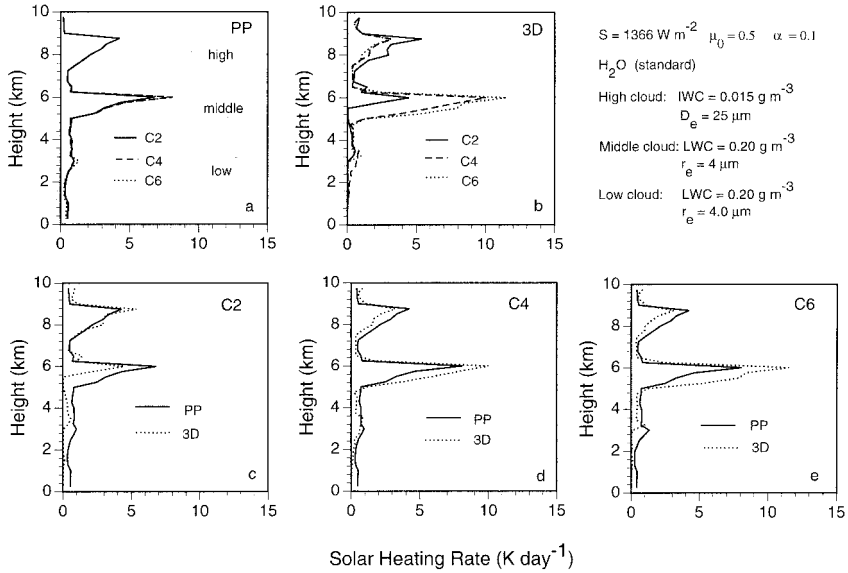

FIG. 12. Solar heating rates calculated from (a) the PP method and (b) the 3D model for different cloud overlaps, and comparisons between the PP method (solid) and the 3D model (dashed) for (c) two columns, (d) four columns, and (e) six columns.

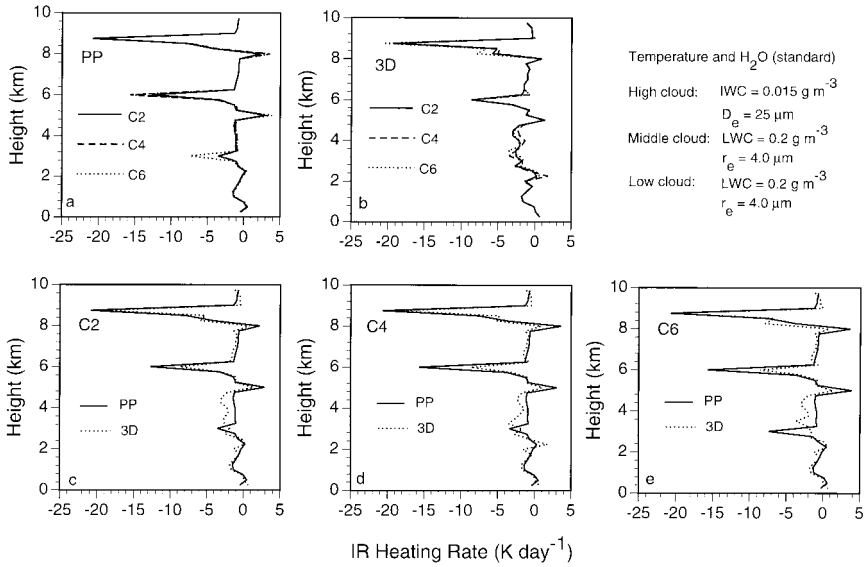

FIG. 13. The IR cooling rates calculated from (a) the PP method and (b) the 3D model for different cloud overlaps, and comparisons between the PP method (solid) and 3D model (dashed) for (c) two columns, (d) four columns, and (e) six columns.

ometry effects (Figs. 13c–e). The decrease of IR cooling at the cloud top in the 3D case is at the expense of more IR cooling in clear sky.

The net heating rate profiles are displayed in Fig. 14. Substantial differences are shown in the middle cloud level between maximum overlap and the other two configurations for the 3D case (Fig. 14b). Maximum overlap displays net cooling at the cloud top and heating at the cloud bottom. Four- and six-column cloud configurations produce net heating within the cloud. Differences in net heating rates between the 3D and PP models are smaller for clouds with maximum overlap than in the two other configurations. For clouds with random overlap, results from these two models differ primarily in the middle cloud level. Net heating within the cloud is seen in the 3D simulation, but cooling at the cloud top and heating at the cloud bottom are shown in the PP calculations (Figs. 14c–e).

Effects of broken clouds on radiative transfer have been investigated by a number of researchers (Harshvardhan and Weinman 1982; Coakley and Kobayashi 1989; Barker and Davies 1992). The solar albedo and

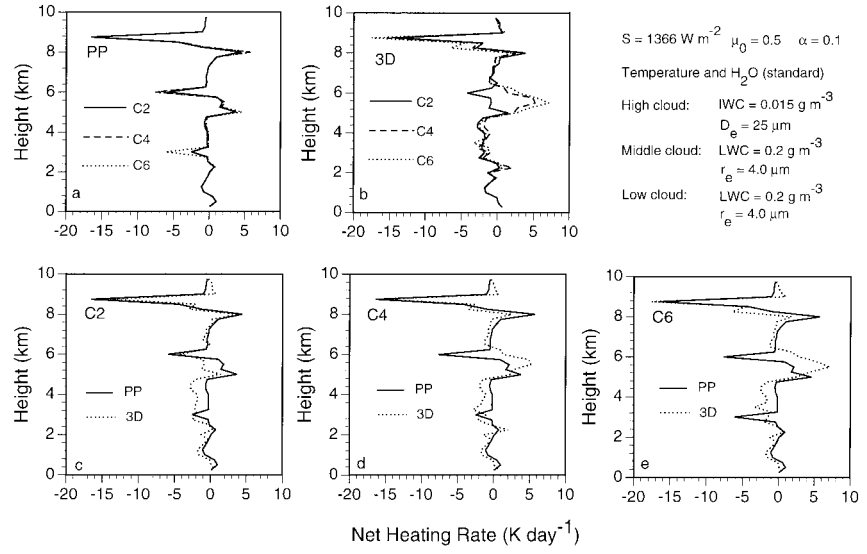

FIG. 14. Net heating/cooling rates calculated from (a) the PP method and (b) the 3D model for different cloud overlaps, and comparisons between the PP method (solid) and 3D model (dashed) for (c) two columns, (d) four columns, and (e) six columns.

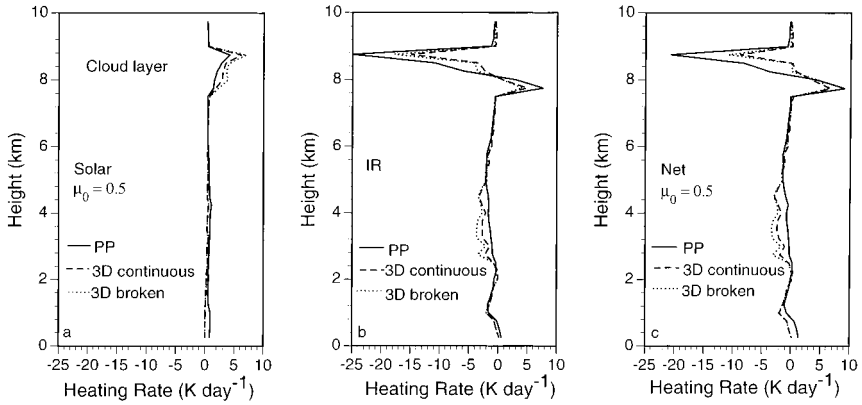

FIG. 15. (a) Solar heating, (b) IR cooling, and (c) net heating/cooling rates calculated from the PP (solid) and 3D model for a continuous cloud field (dashed) and broken clouds (dotted).

IR emissivity of a broken cloud field differ substantially from that of the plane-parallel counterpart. In this study, we have carried out calculations for a single-level continuous cloud and broken clouds employing the configurations displayed in Figs. 10d and 10e. The total cloud cover in these two cases is 60%. While the results computed from the PP model are exactly the same for both cases, those from the 3D model show significant differences (Fig. 15). For solar radiation, broken clouds appear to produce more heating in the cloud layer because the possibility of photons reflected by one broken cloud and intercepted by another is higher than in the PP case. Broken clouds also show more IR cooling at the cloud top (Fig. 15b). This is in line with the calculations of longwave radiative cooling rate in three-dimensional clouds performed by Liou and Ou (1979) and Guan et al. (1995), which demonstrated that cloud-side cooling is of the same order of magnitude as cloud-top cooling for a finite cloud. The cloud-side longwave cooling may significantly affect cloud development by producing enhanced downward motion near cloud sides and upward motion near the center of the cloud (Guan et al. 1997). The differences between the 3D and PP models in this case are mainly due to the cloud geometry effects, as noted previously.

5. Conclusions

A radiative transfer model based on the diffusion approximation approach has been developed to simulate the transfer of radiation in 3D inhomogeneous cirrus clouds. The extinction coefficient, single-scattering albedo, and asymmetry factor are functions of the wavelength and spatial position, and can be parameterized in terms of IWC and mean effective ice crystal size. The delta-function adjustment is used to account for the forward diffraction peak in the phase function to enhance computational accuracy. The second-order partial differential transfer equations with proper boundary conditions imposed are solved numerically by using an efficient overrelaxation method. Comparisons of the model results with those from PP and other 3D models show reasonable agreement for both monochromatic and broadband computations.

The PP method is shown to be a good approximation under the homogeneous condition when the cloud horizontal dimension is much larger than its thickness. As the horizontal dimension decreases, clouds produce less IR warming at the bottom as well as less cooling at the top, while generating more solar heating within the cloud. For inhomogeneous cases, upwelling and downwelling fluxes illustrate patterns associated with the extinction coefficient field. Moreover, cloud inhomogeneity plays an important role in determining heating rate distributions for both solar and IR radiation.

We apply the present radiation parameterization for 3D inhomogeneous clouds to climate model studies in terms of domain-averaged heating and cooling rates. Simulation results for a variety of cloud overlaps show that the cloud vertical structure plays a critical role in the determination of domain-averaged solar heating rates. Clouds with random overlap tend to produce more heating than those with maximum overlap. For IR, the differences between the 3D and PP models are produced primarily from finite cloud geometry effects. The way in which clouds overlap is of less significance, however. Last, we show that broken clouds produce more solar heating as well as more IR cooling as compared with a continuous cloud field.

Acknowledgments. Research supported by DOE Grants DE-FG03-98ER62526 and DE-FG03-00ER62904 and NSF Grants ATM-9796277 and ATM-9907924. The authors thank Dr. Frank Evans for providing the input data from LES model simulated cloud and radiation results for comparisons of the present 3D inhomogeneous radiative transfer model with the SHDOM method.

REFERENCES

Barker, H. W., and J. A. Davies, 1992: Solar radiative fluxes for broken cloud fields above reflecting surfaces. *J. Atmos. Sci.,* **49,** 749–761.

——, G. L. Stephens, and Q. Fu, 1999: The sensitivity of domain-averaged solar fluxes to assumptions about cloud geometry. *Quart. J. Roy. Meteor. Soc.,* **125,** 2127–2152.
Cahalan, R., W. Ridgway, and W. Wiscombe, 1994: Independent pixel and Monte Carlo estimates of stratocumulus albedo. *J. Atmos. Sci.,* **51,** 3776–3790.
Chou, M. D., M. J. Suarez, C. H. Ho, M. M.-H. Yan, and K.-T. Lee, 1998: Parameterizations for cloud overlapping and shortwave single-scattering properties for use in general circulation and cloud ensemble models. *J. Climate,* **11,** 202–214.
Coakley, J. A., Jr., and T. Kobayashi, 1989: Broken cloud biases in albedo and surface insolation derived from satellite imagery data. *J. Climate,* **2,** 721–730.
Davies, R., W. L. Ridgway, and K. Kim, 1984: Spectral absorption of solar radiation in cloudy atmospheres: A 20 cm^{-1} model. *J. Atmos. Sci.,* **41,** 2126–2137.
Donner, L. J., C. J. Seman, B. J. Soden, R. S. Hemler, J. C. Warren, J. Strom, and K.-N. Liou, 1997: Large-scale ice clouds in the GFDL SKYHI general circulation model. *J. Geophys. Res.,* **102,** 21 754–21 768.
Evans, K. F., 1993: Two-dimensional radiative transfer in cloudy atmosphere: The spherical harmonic spatial grid method. *J. Atmos. Sci.,* **50,** 3111–3124.
——, 1998: The spherical harmonics discrete ordinate method for three-dimensional atmospheric radiative transfer. *J. Atmos. Sci.,* **55,** 429–446.
Fu, Q., and K. N. Liou, 1992: On the correlated *k*-distribution method for radiative transfer in nonhomogeneous atmospheres. *J. Atmos. Sci.,* **49,** 2139–2156.
——, and ——, 1993: Parameterization of the radiative properties of cirrus clouds. *J. Atmos. Sci.,* **50,** 2008–2025.
——, M. C. Cribb, H. W. Barker, S. K. Krueger, and A. Grossman, 2000: Cloud geometry effects on atmospheric solar absorption. *J. Atmos. Sci.,* **57,** 1156–1168.
Gabriel, P. M., S. C. Tsay, and G. L. Stephens, 1993: A Fourier–Riccati approach to radiative transfer. Part I: Foundations. *J. Atmos. Sci.,* **50,** 3125–3147.
Geleyn, J. F., and A. Hollingsworth, 1979: An economical analytical method for the computation of the interaction between scattering and line absorption of radiation. *Contrib. Atmos. Phys.,* **52,** 1–16.
Guan, H., R. Davies, and M. K. Yau, 1995: Longwave radiative cooling rates in axially symmetric clouds. *J. Geophys. Res.,* **100,** 3213–3220.
——, M. K. Yau, and R. Davies, 1997: The effects of longwave radiation in a small cumulus cloud. *J. Atmos. Sci.,* **54,** 2201–2214.
Harshvardhan, and J. A. Weinman, 1982: Infrared radiative transfer through a regular array of cuboidal clouds. *J. Atmos. Sci.,* **39,** 431–439.
Heymsfield, A. J., and L. M. Miloshevich, 1993: Overview of microphysics and state parameter measurements from FIRE-II. *Proc. Conf. on FIRE Cirrus Science Results 1993,* Breckenridge, CO, NASA, 1–4.
Hignett, P., and J. P. Taylor, 1996: The radiative properties of inhomogeneous boundary layer clouds: Observations and modeling. *Quart. J. Roy. Meteor. Soc.,* **122,** 1341–1364.
Liang, X.-Z., and W.-C. Wang, 1997: Cloud overlap effects on general circulation model climate simulations. *J. Geophys. Res.,* **102,** 11 039–11 047.
Liou, K. N., 1986: Influence of cirrus clouds on weather and climate processes: A global perspective. *Mon. Wea. Rev.,* **114,** 1167–1199.
——, 1992: *Radiation and Cloud Processes in the Atmosphere: Theory, Observation, and Modeling*. Oxford University Press, 487 pp.
——, and S. C. Ou, 1979: Infrared radiative transfer in finite cloud layers. *J. Atmos. Sci.,* **36,** 1985–1996.
——, and N. Rao, 1996: Radiative transfer in cirrus clouds. Part IV: On cloud geometry, inhomogeneity, and absorption. *J. Atmos. Sci.,* **53,** 3046–3065.
——, P. Yang, Y. Takano, K. Sassen, T. Charlock, and W. P. Arnott, 1998: On the radiative properties of contrail cirrus. *Geophys. Res. Lett.,* **25,** 1161–1164.
Minnis, P., K. N. Liou, and Y. Takano, 1993: Inference of cirrus cloud properties using satellite-observed visible and infrared radiances. Part I: Parameterization of radiance field. *J. Atmos. Sci.,* **50,** 1279–1304.
Moeng, C.-H., and Coauthors, 1996: Simulations of a stratocumulus-topped planetary boundary layer: Intercomparison among different numerical codes. *Bull. Amer. Meteor. Soc.,* **77,** 261–278.
Morcrette, J. J., and Y. Fouquart, 1986: The overlapping of cloud layers in shortwave radiation parameterization. *J. Atmos. Sci.,* **43,** 321–328.
O'Hirok, W., and C. Gautier, 1998: A three-dimensional radiative transfer model to investigate the solar radiation within a cloudy atmosphere. Part I: Spatial effects. *J. Atmos. Sci.,* **55,** 2162–2179.
Ou, S. C., and K. N. Liou, 1982: Generalization of the spherical harmonic method to radiative transfer in multi-dimensional space. *J. Quant. Spectrosc. Radiat. Transfer,* **28,** 271–288.
——, and Coauthors, 1995: Remote sounding of cirrus cloud optical depths and ice crystal sizes from AVHRR data: Verification using FIRE II IFO measurements. *J. Atmos. Sci.,* **52,** 4143–4158.
Rigal, A., 1979: Convergence and optimization of successive over-relaxation for linear system of equation with complex eigenvalues. *J. Comput. Phys.,* **32,** 10–23.
Sassen, K., 1991: The polarization lidar technique for cloud research: A review and current assessment. *Bull. Amer. Meteor. Soc.,* **72,** 1848–1886.
Spinhirne, J. D., and W. D. Hart, 1990: Cirrus structure and radiative parameters from airborne lidar and spectral radiometer observations: The 28 October 1986 FIRE study. *Mon. Wea. Rev.,* **118,** 2329–2343.
Stephens, G. L., and S.-C. Tsay, 1990: On the cloud absorption anomaly. *Quart. J. Roy. Meteor. Soc.,* **116,** 671–704.
Stubenrauch, C. J., A. D. Del Genio, and W. B. Rossow, 1997: Implementation of subgrid cloud vertical structure inside a GCM and its effect on the radiation budget. *J. Climate,* **10,** 273–287.
Tian, L., and J. A. Curry, 1989: Cloud overlap statistics. *J. Geophys. Res.,* **94,** 9925–9935.
Wylie, D. P., W. P. Menzel, H. M. Woolf, and K. I. Strabala, 1994: Four years of global cirrus cloud statistics using HIRS. *J. Climate,* **7,** 1972–1986.